Super-Variable Focusing Vortex Beam Generators Based on Spiral Zone Plate Etched on Optical Fiber Facet

Jian Yu, Cailing Fu, Zhiyong Bai, and Yiping Wang, *Senior Member, IEEE, Senior Member, OSA*

***Abstract*—In this article, an all-fiber super-variable focusing vortex beam generator is proposed and demonstrated, the focal point of which can be drastically relocated by varying the wavelength of the incident light. The all-fiber generator is fabricated by etching a spiral zone plate (SZP) on the top of the composite fiber structure composed of a single mode fiber and a quarter pitch graded index fiber using focused ion beam lithography. Numerical simulation and experimental measurements have been applied in investigation of all-fiber output light field characteristics, such as the focal spot, focal length, and vortex topological charges. Results show that these parameters can be controlled by flexibly adjusting the design parameters of SZP microstructure. In particular, the position of the donut-shaped focus spot can be dynamically tuned in a wide range by varying the incident laser wavelength with the focal spot profile remains constant. The all-fiber generator can be potentially applied in particle manipulation, high capacity communication, and fiber optic endoscopic imaging, all of which require ultra-compact, multi-dimension, and flexible focusing schemes.**

***Index Terms*—Fiber facet, focused ion beam, spiral zone plate, vortex beam.**

I. Introduction

VORTEX beam has attracted widespread attention due to its unique physical properties, such as phase singularity, donut-shaped field distribution, and intrinsic orbital angular momentum (OAM) [1]–[3]. In recent years, vortex beam has been widely used in particle manipulation [4], super-resolution microscopy [5], high capacity communication [6], and astronomical observation [7]. In the past two decades, the techniques for generating vortex beam are mainly based on various optical devices involving free-space beam propagation, including spatial light modulators [8], cylindrical lens mode converters [9], compact metamaterials [10], and spiral phase plates [11]. In recent years, fiber-based photonic integration has become a major propellant for widespread application of vortex beam due to its advantages in reliability, miniaturization, and scalability compared to bulk optics. Researchers have developed various all-fiber vortex beam generators based on different working principles such as multimode interference [12], acoustic-optic interaction [13], stress-induced phase difference [14]. Moreover, diverse optical fibers selections provide multiple solutions for vortex beams generation and application, such as single-mode fibers (SMF) [15], few-mode fibers [14], [16], photonic crystal fibers [17], and other special types of fibers [18]–[20]. These fiber-based generators have been perceived as an effective alternative to traditional free-space vortex beam generating devices.

Directly integrating photonic devices onto an optical fiber facet is an extremely important way to generate vortex beams as no special design or external control is required for fibers. However, it is usually very challenging to integrate a good-performance vortex light generating photonic device onto an optical fiber facet with a diameter of 125 μm or less. Weber *et al.* reported that a spiral staircase phase plate can be modified on top of an SMF via 3D direct laser writing and further polymerization to generate OAM light [21]. The patterning of similar structures on an SMF facet using focused ion beam (FIB) lithography was also investigated by Vayalamkuzhi and R. S. Rodrigues Ribeiro *et al.* [22], [23]. In addition, Xie *et al.* [24] developed an OAM multiplexer by integrating Damman vortex grating on the top of a few-mode fiber with femtosecond laser two-photon polymerization. These several research works have successfully realized the effective generation of vortex beams.

Spiral zone plate (SZP) is a typical hybrid diffractive optical element that is often used to generate a focused vortex beam in a single step [3], [25]. Usually, an SZP is designed by binarizing a computer-generated hologram, which is formed through the coherent interference of spherical wave and vortex beam. Although SZPs fabricated on different substrates have been widely

Manuscript received August 11, 2020; revised November 4, 2020; accepted November 12, 2020. Date of publication November 17, 2020; date of current version March 1, 2021. This work was supported in part by the National Natural Science Foundation of China under Grant 61875134, Grant 61425007, and Grant 61905166; and in part by the Science and Technology Innovation Commission of Shenzhen under Grant JCYJ20180507182058432, Grant JCYJ20170818143853289, Grant JCYJ20180305125352956, and Grant JCYJ20160427104925452. *(Corresponding author: Zhiyong Bai.)*

Jian Yu is with the Key Laboratory of Optoelectronic Devices and Systems of Ministry of Education and Guangdong Province, College of Optoelectronic Engineering, Shenzhen University, Shenzhen 518060, China, and also with the Guangdong and Hong Kong Joint Research Centre for Optical Fiber Sensors, Shenzhen University, Shenzhen 518060, China (e-mail: yujian@szu.edu.cn).

Cailing Fu is with the Guangdong and Hong Kong Joint Research Centre for Optical Fiber Sensors, Shenzhen University, Shenzhen 518060, China (e-mail: fucailing@szu.edu.cn).

Zhiyong Bai is with the Guangdong and Hong Kong Joint Research Centre for Optical Fiber Sensors, Shenzhen University, Shenzhen 518060, China, and also with the Shenzhen Key Lab of Photonic Devices and Sensing Systems for Internet of Things, Shenzhen University, Shenzhen 518060, China (e-mail: baizhiyong@szu.edu.cn).

Yiping Wang is with the Guangdong and Hong Kong Joint Research Centre for Optical Fiber Sensors, Shenzhen University, Shenzhen 518060, China, and also with Shenzhen Photonic Sensing Technology Co. Ltd., Shenzhen 518100, China (e-mail: ypwang@szu.edu.cn).

Color versions of one or more of the figures in this article are available online at https://doi.org/10.1109/JLT.2020.3038650.

Digital Object Identifier 10.1109/JLT.2020.3038650

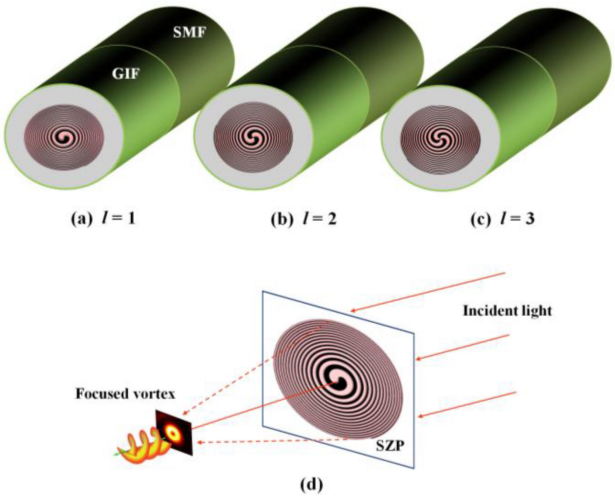

Fig. 1. (a, b, c) Schematic showing the focusing vortex beam generators for $l = 1$, 2, and 3, respectively. (d) SZP generating a focused vortex beam with helical wavefronts in a single step.

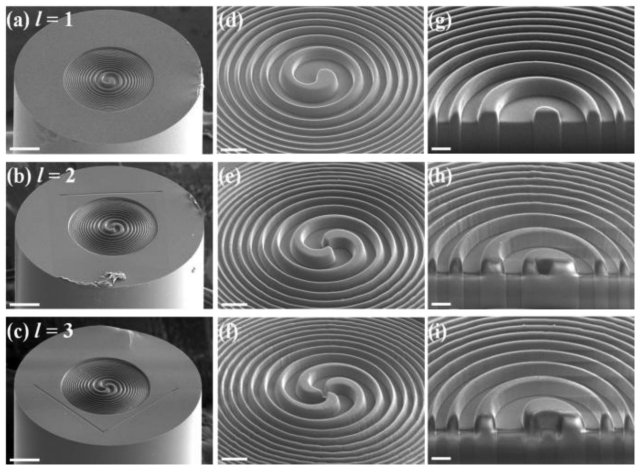

Fig. 2. (a, b, c) SEM images of the overall fiber facet structure for $l = 1$, 2, and 3. (d, e, f) Magnified images from the central region in the milled SZP structure. (g, h, i) Cross section images from the central region in the milled SZP structure. Scale bars in (a–c), (d–f), and (g–i) are 20, 10 and 5 μm, respectively.

reported for use in various applications [26], [27], few studies have focused on addressing the microstructure fabricated on an optical fiber facet. Very recently, we have reported on the research work of fabricating SZP on an optical fiber based on femtosecond laser two-photon polymerization technology [28]. This type of fiber-based SZP has been proven to directly generate focused vortex beams without the need for additional focusing optics. However, the polymerized SZP microstructure on the top of the optical fiber is easy to fall off, especially when used in some organic solvents or in a strong disturbance environment, which has severely limited its application.

In this paper, we report a novel all-fiber focusing vortex beam generator that fabricated by directly etching the SZP microstructure on an optical fiber facet with FIB lithography. The all-fiber focusing vortex beam generators exhibit excellent performance in terms of mechanical robustness and optical stability due to the unique SZP microstructure, of which the microstructure is hidden inside the fiber consisting of the same material with fiber. Specifically, we further explored how the super-variable vortex focusing functionality change as the wavelength of incident light changed systemically. The all-fiber super-variable focusing vortex beam generators can be potentially applied in particle manipulation, optical fiber communication and optical fiber imaging.

II. Design and Fabrication

Fig. 1(a)–1(c) show the structure diagrams of the proposed all-fiber super-variable focusing vortex beam generators. An 80 mm long SMF (8.2/125 μm, Corning G652D) was first spliced to a segment of graded-index multimode fiber (GIF) (62.5/125 μm, Yangtze Optical Fiber GI0.275). And then, the GIF was cut to a quarter-pitch length (245 μm) with a computer-controlled fiber precision cleaving system [29]. Subsequently, the binarized SZP microstructures with different numbers of spiral arms ($l = 1$, 2, and 3) were etched onto the GIF facet using FIB lithography, respectively. The fundamental mode propagating in the SMF was expanded and collimated in the GIF segment, and then the etched SZP modulated the collimated light into a focusing vortex beam. The SZP was designed to operate at $\lambda = 1550$ nm with a focal length $f = 20$ μm, diameter size $d = 62.5$ μm, and etch depth $h = 1.582$ μm. Here the etch depth was set to a fixed value with refractive index $n = 1.490$, because the inequality or relative deviation of the refractive index at any position of the GIF core region has little effect on the output light field characteristics. Fig. 1(d) shows schematic diagram of the working principle of the SZP generating a focused vortex beam. The SZP realizes continuous spiral phase wavefront and convergence effect of its output beam in a single step by modifying the annular-shaped zone distribution of traditional FZP microstructure to spiral-shaped zone distribution. Essentially, the spiral distribution causes the optical path from SZP itself to its focal plane to vary with the azimuthal angle, and finally produces a donut-shaped focal spot with OAM and spiral phase wavefront.

In order to prevent charging during FIB etching, an Au layer of 10 nm thickness was first deposited to the flat-cleaved facet of the GIF using an electron-beam evaporation system. The deposited fiber sample was then firmly attached to the sample stage of the dual beam FIB Nova Nanolab 600 (FEI) system with conductive adhesive. The multi-dimensional pose control platform of the FIB system was used to precisely adjust the sample stage position for realizing an accurate etching. Pattern files were generated using MATLAB software and stored as bitmap images, which were imported into the FIB system for etching. A serpentine scanning strategy with bottom-to-top scan direction was used to etch the SZP microstructure. It is crucial to optimize the process parameters to ensure the etching accuracy, etching depth, and moderate etching duration. After many exploratory experiments, we found that a 30 keV acceleration voltage, 5 nA beam current, 1 μs dwell time, and 600 nm depth value Z can etch a relatively good SZP microstructure. The depth value Z corresponds to an etching duration of 39 min 47 s, which was calculated using the Au material file from the dual beam software database. The scanning electron microscopy (SEM) images of

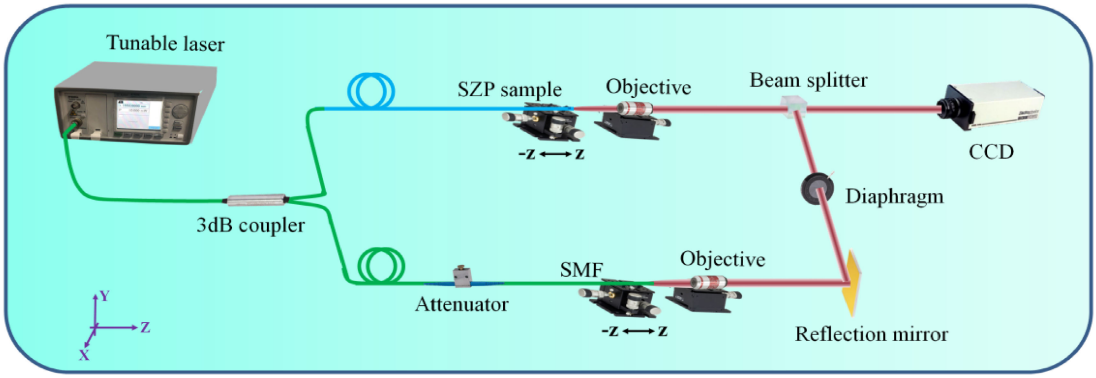

Fig. 3. Dual-beam interference microscopic imaging system.

the etched SZP microstructure on the fiber facet are shown in Figs. 2(a)–2(c). The magnified images from the central region of the etched SZP microstructures are shown in Figs. 2(d)–2(f). As we can see, the etched microstructures are not a perfect binary morphology because a large ion beam current was used for etching in order to reduce the etching duration. In order to obtain the actual etching depth, the SZP microstructures were etched along its normal direction using a larger ion beam current (7 nA). The cross section images are shown in Figs. 2(g)–2(i), corresponding to $l = 1$, 2, and 3, respectively. The measured depth value is 1.577 μm, which is very close to the desired value of 1.582 μm.

III. Characteristics

A dual-beam microscopic imaging system was constructed to characterize the vortex focusing behavior of the fabricated all-fiber generator. As shown in Fig. 3, a tunable laser with an emission wavelength ranging from 1520 to 1630 nm was first connected to a 3 dB coupler. One output port of the 3 dB coupler was connected to the virgin end of the SZP sample for generating the desired focusing vortex beam from its rear end, and the other output port was connected to an SMF for generating a reference beam. The rear ends of the SMF and SZP sample were fixed on a micromanipulation stage that can be moved horizontally from –Z to Z direction with micrometer precision. A 40× objective lens was used to magnify the output beams from the SMF and SZP sample. Meanwhile, a beam splitter was placed at the intersection between the two magnified beams, and the non-coaxial interference patterns from the two beams were observed using an infrared CCD camera. When the reference beam was blocked, the camera only captured the output beam from the SZP samples.

In order to verify the occurrence of vortex focusing, the light field distribution near the focus point of the SZP sample was first investigated by blocking the reference beam with a diaphragm. The operating wavelength of the tunable laser was set to 1550 nm. The SZP sample was moved along the optical axis by adjusting the micromanipulation stage, and the intensity distribution of the output beam in the horizontal plane (X, Y) were observed using the infrared CCD camera at different longitudinal position Z. Here, the smallest focus spot position of the output beam was considered to be the focus point (or initial position). And then, the micromanipulation stage was moved in 5 μm sampling increment toward -Z or Z direction. Meantime, the output light field distributions of the SZP sample with different l number were simulated by finite difference time domain (FDTD) algorithm. A circularly polarized Gaussian beam with a wavelength of 1550 nm and beam waist of 10 μm was defined as the incident light field and it was then impinged onto the SZP microstructure at normal incidence. Similarly, other simulation parameters were also set to closely match those in the experiment.

Fig.s 4(a)–4(c) show the intensity distributions of different SZP sample ($l = 1$, 2, and 3) obtained from simulations and experiments. As we can see from the simulations, the output light intensity distributions of all SZP samples in the focus area exhibit a two-lobed shape along the longitudinal direction in the range of Z = 0 to 32 μm. The two lobes of light intensity were quasi-symmetrically distributed on both sides of the optical axis. Moreover, the spacing between the two lobes increases as l increases. The white vertical dotted lines represent the different sampling positions along the longitudinal direction. Just below each white dotted line, the corresponding light field intensity distribution obtained from FDTD simulation and experimental measurement are presented, respectively. Here, the simulation and measurement results maintain a high degree of consistency. All SZP samples focus their output beam to a small donut-shaped intensity pattern at the back focal plane. The focal spot size gradually increases as l is changed from 1 to 3. Corresponding to $l = 1$, 2, and 3, the diameters of focal spot obtained from simulation are 3.7, 4.8, and 6.1 μm, respectively. The measured values in the experiment are 3.5, 4.7, and 6.0 μm, respectively, which match the simulation results very well. Further simulation results show that the focal spot diameter continues to increase as l increases.

Noticeably, the broken axisymmetry of the donut-shaped focal spots at the focal plane can be observed both from the simulation and experiments. Its origin is attributed to the finite beam size irradiated to the SZP microstructure. In fact, the GIF with a quarter-pitch length only expanded the fundamental mode propagating in the SMF to a 25 μm diameter according

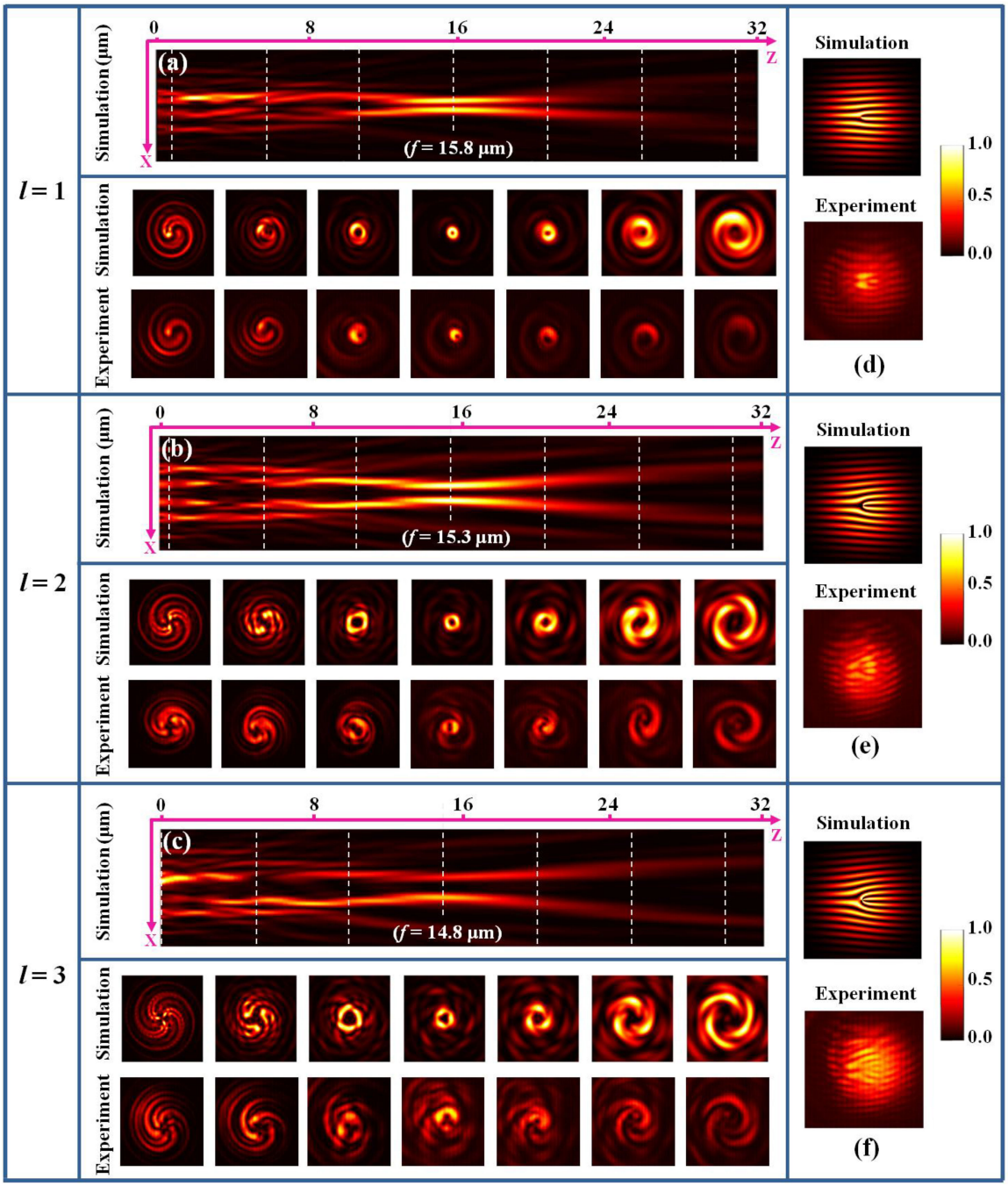

Fig. 4. (a, b, c) FDTD simulated intensity cross-sections in the longitudinal plane (X, Z), and intensity cross-section in the different horizontal sampling planes (X, Y) determined from FDTD simulations and experimental measurements, respectively. (d, e, f) Simulated and measured non-coaxial interference patterns between the output-coupled light and reference beam, respectively.

to our experimental measurement results. The finite beam size is equivalent to an abrupt end of the SZP's spiral arm at the periphery of the incident beam. In this situation, the focal spot is evolved into a donut-shaped intensity pattern composed of multiple petals as l increases. To improve the axisymmetry, we need to further expand the effective size of the incident beam using a GIF fiber with a larger core diameter.

When the SZP sample was moved towards the objective lens, its microstructure profile was clearly projected onto the CCD camera. The focal length of the SZP sample is perceived as the distance between the focal point and the special point where the SZP profile was clearly imaged. For $l = 1$, 2, and 3, the focal length obtained from experiments are 16.0, 15.4, and 14.7 μm, respectively. Corresponding simulation results are 15.8, 15.3, and 14.8 μm, respectively, as noted in Figs. 4(a)–4(c). Here the slight discrepancy between the simulation and measurement is attributed to the machining error and measurement error. It is worth noting that there is a large discrepancy between the

simulated (or measured) focal length and the designed focal length ($f = 20$ μm). This discrepancy may be attributed to diffraction of the evanescent field inside the subwavelength features of the SZP microstructure [30]. In addition, the vortex topological charge of the output focused beam was investigated using non-coaxial interference with the reference beam from SMF. Figs. 4(d)–4(f) show the interferograms obtained from the simulation and experiment, respectively. The simulation results are supported by the experiments. All interferograms exhibit a dislocated fringe-shaped pattern, which confirms that the output focused beam carries OAM and spiral phase. The number of the dislocated fringe represents the vortex topological charge value carried by the output beam.

As a hybrid diffractive optical element, an SZP is perceived as a combination of a spiral phase plate and traditional FZP. The spiral phase plate can modulate the propagating beam in the GIF segment into a vortex beam carrying spiral phase and OAM. The FZP can focus the propagating beam in the GIF into a small spot, and its super-variable focusing functionality has been confirmed in theory and via experiments by Kim *et al.* [31]. Combining the two components, the SZP etched on the GIF facet are expected to have a super-variable vortex focusing functionality. According to Ref. [3], the boundary of the planar spiral-shaped zone of the binarized SZP can be determined by the following mathematical formula:

$$l\theta = (n + 1/2)\,\pi + \frac{\pi r^2}{\lambda_0 f_0}, \tag{1}$$

where $n = 0, \pm1, \pm2, \ldots, (r, \theta)$ refer to the polar coordinates, n denotes the ring number of the spiral-shaped zone, k is vacuum wavenumber related to the incident wavelength λ_0 through $k = 2\pi/\lambda_0$, ℓ and f_0 represent the numbers of spiral arms and the nominal focal length, respectively. Once all the geometric parameters $(l, n, (r, \theta))$ of the SZP microstructure are determined for a fixed parameter set of λ_0 and f_0, detuning of the incident wavelength will subsequently lead to a shift of the focal point, because $\lambda_0 f_0$ is a fixed value. As illustrated in Fig. 5, the elongation of the incident wavelength gives rise to increase of the optical path difference between two adjacent spiral slits (see Δl in Fig. 5) in order for keeping the constructive interference condition at the target point. This subsequently leads to a considerable amount of shift of the focal point towards the SZP. One can also estimate the change of the focal point with respect to the incident wavelength from the Eq. (1). Assuming that the focal length is substantially longer than the incident wavelength, the product of the wavelength and the corresponding focal length becomes approximately invariant for a fixed SZP geometry. When the incident wavelength is substantially detuned to a new wavelength λ, the equation: $\lambda f_\lambda = \lambda_0 f_0$ can always be satisfied, and the new focal length f_λ for the detuned wavelength λ is determined by

$$f_\lambda = \frac{\lambda_0 f_0}{\lambda}. \tag{2}$$

As a result, an SZP has a super-variable vortex focusing characteristic feature that its focal length becomes inversely proportional to the incident wavelength.

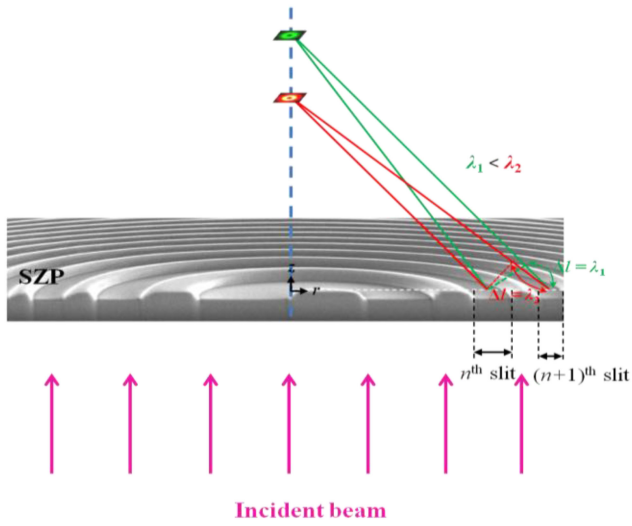

Fig. 5. Principle of the focal-point shift of an SZP with respect to the incident wavelength.

To verify the variable vortex focusing functionality of the fabricated all-fiber generators, we have performed FDTD simulations and gathered experimental measurements using different incident laser wavelengths for the case of $l = 1$ and 2. In Fig. 6, the images in the first row show the measured intensity distribution of the focused spots, the images in the second row show the measured interferograms between the output focused beam and reference beams, and the images in the third row show the simulated longitudinal intensity distribution near the focal point. As we can see, the focal spot of each SZP sample is almost unchanged when the incident laser wavelength was adjusted from 1530 to 1570 nm in 10 nm increments. Simultaneously, all interferograms with dislocated fringes show that the output beams maintain their vortex topological charge. As the incident wavelength increases, the focal length of the all-fiber generators gradually decreases, which can be clearly seen through the blue horizontal line and pink slanted arrow in the third row of images. There is a slight difference in slope for different numbers of spiral arms l when the focal length varies with the incident wavelength. For $l = 1$, the focal length varies quasi-linearly from 15.95 to 15.40 μm. For $l = 2$, the focal length quasi-linearly varies from 15.80 to 15.50 μm. Since the material dispersion from the GIF is extremely low, its influence on the change of focal length with incident wavelength is negligible. That is, the variable focusing functionality of the all-fiber generators comes from the special optical properties of the SZP microstructure. In our experiment, the variable amount is limited by the tunable wavelength range of the laser source. However, in theory, the all-fiber generators have the ability to realize a wider variable vortex focusing range.

To explore the super-variable vortex focusing functionality, we have performed further numerical simulation analysis using a wider incident wavelength range for the case of $l = 1$ and 2. The incident wavelength was set from 1200 to 2000 nm with an interval of 100 nm. As shown in Fig. 7(a), the focal lengths of the all-fiber generators ($l = 1$ and 2) gradually decreases when

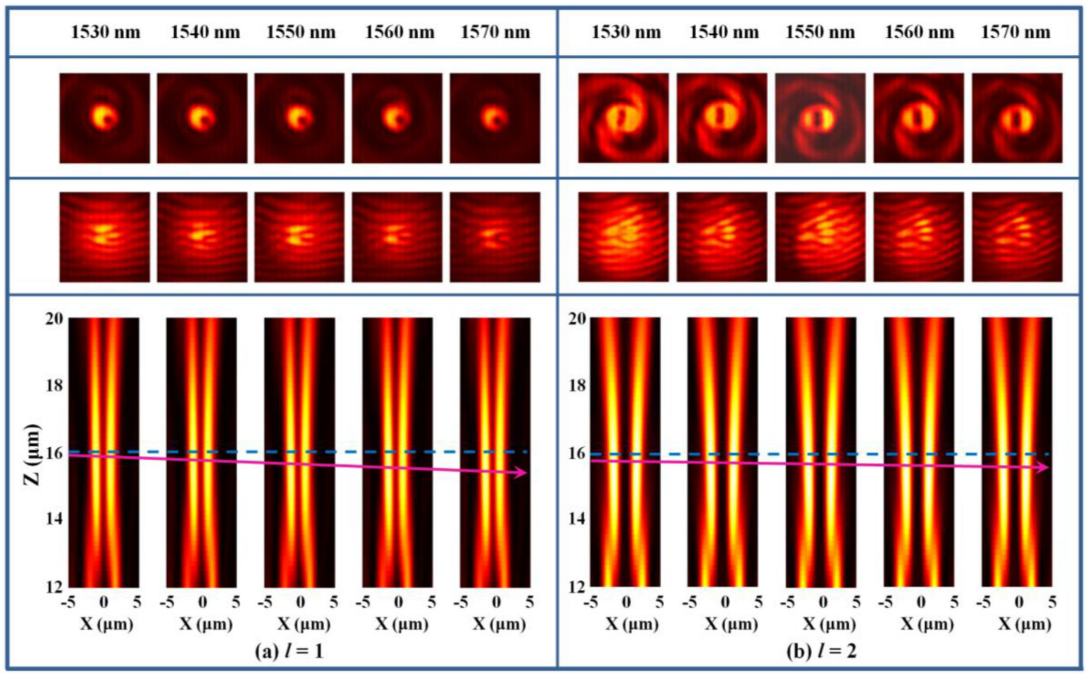

Fig. 6. Variable vortex focusing characteristics for the wavelength range from 1530 to 1570 nm. (a) $l = 1$, (b) $l = 2$.

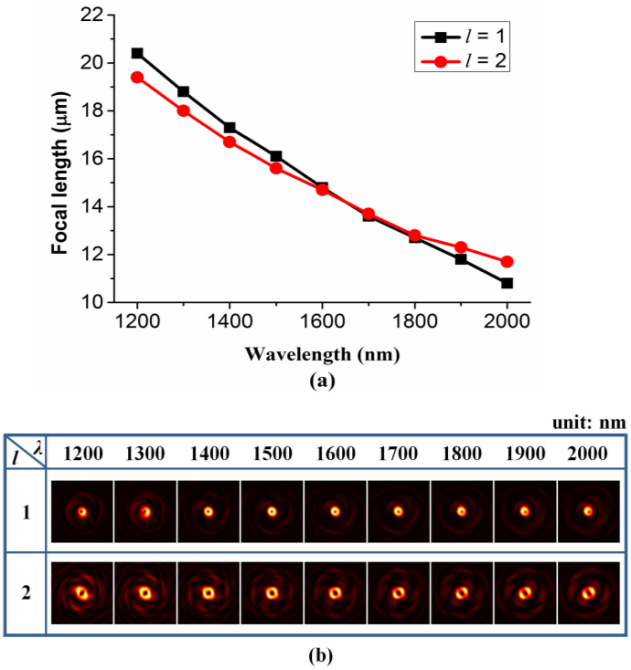

Fig. 7. (a) The focal length value of the all-fiber generator under different incident laser wavelengths for the case of $l = 1$ and 2. (b) The intensity profile of the focused spot of the all-fiber generator corresponding to different incident laser wavelengths for the case of $l = 1$ and 2.

the incident wavelength increases. Moreover, the focal length change in the two cases is obviously different. When $l = 1$, the focal length is decreased from 20.4 to 10.8 μm, and the variable amount is 9.6 μm. When $l = 2$, the focal length is decreased from 19.4 to 11.7 μm, and the corresponding variable amount is 7.7 μm. Meanwhile, the focal spot profile of each SZP fiber sample maintains approximately invariant behavior in the wide incident wavelength range, as shown in Fig. 7(b). Therefore, it can be concluded that the all-fiber generators can realize a super-variable vortex focusing functionality by adjusting the incident laser wavelength while keeping their focal spot profile almost unchanged. When the incident wavelength is far from the initial design wavelength 1550 nm, for example, the deviation value $\Delta\lambda > 400$ nm, the donut-shaped focal spot profile will exhibit a slightly more obvious degradation, especially towards the direction of short waves. The maximum amount of focal length change in use is essentially determined by the specific requirements for the donut-shaped focal spot profile.

IV. Conclusion

In summary, we have successfully prepared SZP with the number of spiral arms $l = 1$, 2, and 3 on the top of the composite fiber structure (SMF + GIF) using FIB lithography. Numerical simulation and experimental measurements demonstrated that the all-fiber generator can generate focused beams carrying vortex topological charges of 1, 2, and 3, respectively, in a single step. Moreover, the characteristics of the output focused vortex beam, such as focal spot size, focal length, and topological charge, can be easily manipulated by flexibly changing the design parameters of the SZP microstructure. In addition, the super-variable characteristics of the focal length have been confirmed using different incident laser wavelengths. For the case of $l = 1$ and 2, the variable amount of the focal length reach to 9.6 and 7.7 μm, respectively, when the incident wavelength changes from 1200 to 2000 nm. Moreover, the variable amount will be much larger if we further relax the requirements for the

focus spot profile. This super-variable vortex focusing generator can be applied in many fields, such as the multi-dimensional particle manipulation with a long-range working distance, and the broadband OAM communication with a high coupling efficiency.

REFERENCES

[1] M. J. Padgett, "Orbital angular momentum 25 years on invited," *Opt. Express*, vol. 25, no. 10, pp. 11265–11274, May 2017.

[2] M. J. Padgett, J. Courtial, and L. Allen, "Light's orbital angular momentum," *Phys. Today*, vol. 57, no. 5, pp. 35–40, May 2004.

[3] N. R. Heckenberg, R. McDuff, C. P. Smith, and A. G. White, "Generation of optical phase singularities by computer-generated holograms," *Opt. Lett.*, vol. 17, no. 3, pp. 221–223, Feb. 1992.

[4] M. J. Padgett and R. Bowman, "Tweezers with a twist," *Nat. Photon.*, vol. 5, no. 6, pp. 343–348, Jun. 2011.

[5] G. Vicidomini, P. Bianchini, and A. Diaspro, "STED super-resolved microscopy," *Nat. Methods*, vol. 15, pp. 173–182, Jan. 2018.

[6] L. Liu, Y. Gao, and X. Liu, "High-dimensional vortex beam encoding/decoding for high-speed free-space optical communication," *Opt. Commun.*, vol. 452, pp. 40–47, Dec. 2019.

[7] G. A. Swartzlander, "Peering into darkness with a vortex spatial filter," *Opt. Lett.*, vol. 26, no. 8, pp. 497–499, Apr. 2001.

[8] Y. Ohtake, T. Ando, N. Fukuchi, N. Matsumoto, H. Ito, and T. Hara, "Universal generation of higher-order multiringed Laguerre–Gaussian beams by using a spatial light modulator," *Opt. Lett.*, vol. 32, no. 11, pp. 1411–1413, Jun. 2007.

[9] M. J. Padgett and L. Allen, "Orbital angular momentum exchange in cylindrical-lens mode converters," *J. Opt. B-Quantum S. O.*, vol. 4, no. 2, pp. S17–S19, Apr. 2002.

[10] Z. Zhao, J. Wang, S. Li, and A. E. Willner, "Metamaterials-based broadband generation of orbital angular momentum carrying vector beams," *Opt. Lett.*, vol. 38, no. 6, pp. 932–934, Mar. 2013.

[11] S. Paul *et al.*, "Wavelength-selective orbital-angular-momentum beam generation using MEMS tunable Fabry-Perot filter," *Opt. Lett.*, vol. 41, no. 14, pp. 3249–3252, Jul. 2016.

[12] G. Yin *et al.*, "Orbital angular momentum generation in two-mode fiber, based on the modal interference principle," *Opt. Lett.*, vol. 44, no. 4, pp. 999–1002, Feb. 2019.

[13] W. Zhang *et al.*, "Optical vortex generation with wavelength tunability based on an acoustically-induced fiber grating," *Opt. Express*, vol. 24, no. 17, pp. 19278–19285, Aug. 2016.

[14] S. H. Li, Q. Mo, X. Hu, C. Du, and J. Wang, "Controllable all-fiber orbital angular momentum mode converter," *Opt. Lett.*, vol. 40, no. 18, pp. 4376–4379, Sep. 2015.

[15] C. Fu *et al.*, "Orbital angular momentum mode converter based on helical long period fiber grating inscribed by hydrogen-oxygen flame," *J. Lightw. Technol.*, vol. 36, no. 9, pp. 1683–1688, May 2018.

[16] Y. H. Zhao, Y. Q. Liu, L. Zhang, C. Y. Zhang, J. X. Wen, and T. Y. Wang, "Mode converter based on the long-period fiber gratings written in the two-mode fiber," *Opt. Express*, vol. 24, no. 6, pp. 6186–6195, Mar. 2016.

[17] G. K. L. Wong *et al.*, "Excitation of orbital angular momentum resonances in helically twisted photonic crystal fiber," *Science*, vol. 337, no. 6093, pp. 446–449, Jul. 2012.

[18] Z. Bai *et al.*, "Orbital angular momentum generator based on hollow-core photonic bandgap fiber grating," *Appl. Phys. Express*, vol. 12, no. 7, Jul. 2019, Art. no. 072004.

[19] L. Wang, P. Vaity, B. Ung, Y. Messaddeq, L. A. Rusch, and S. LaRochelle, "Characterization of OAM fibers using fiber bragg gratings," *Opt. Express*, vol. 22, no. 13, pp. 15653–15661, Jun. 2014.

[20] P. Gregg, P. Kristensen, and S. Ramachandran, "Conservation of orbital angular momentum in air-core optical fibers," *Optica*, vol. 2, no. 3, pp. 267–270, Mar. 2015.

[21] K. Weber, F. Huett, S. Thiele, T. Gissibl, A. Herkommer, and H. Giessen, "Single mode fiber based delivery of OAM light by 3D direct laser writing," *Opt. Express*, vol. 25, no. 17, pp. 19672–19679, Aug. 2017.

[22] P. Vayalamkuzhi *et al.*, "Direct patterning of vortex generators on a fiber tip using a focused ion beam," *Opt. Lett.*, vol. 41, no. 10, pp. 2133–2136, May 2016.

[23] R. S. Rodrigues Ribeiro, P. Dahal, A. Guerreiro, P. Jorge, and J. Viegas, "Optical fibers as beam shapers: From Gaussian beams to optical vortices," *Opt. Lett.*, vol. 41, no. 10, pp. 2137–2140, May 2016.

[24] Z. Xie *et al.*, "Integrated (de)multiplexer for orbital angular momentum fiber communication," *Photon. Res*, vol. 6, no. 7, pp. 743–749, Jul. 2018.

[25] A. Balcytis *et al.*, "Hybrid curved nano-structured micro-optical elements," *Opt. Express*, vol. 24, no. 15, pp. 16988–16998, Jul. 2016.

[26] Z. Tian *et al.*, "Mirror-rotation-symmetrical single-focus spiral zone plates," *Opt. Lett.*, vol. 43, no. 13, pp. 3116–3119, Jul. 2018.

[27] Z. Tian, J. Hua, J. Hao, Y. Yu, Q. Chen, and H. Sun, "Micro-buried spiral zone plate in a lithium niobate crystal," *Appl. Phys. Lett.*, vol. 110, no. 4, Jan. 2017, Art. no. 041102.

[28] J. Yu *et al.*, "All-fiber focused beam generator integrated on an optical fiber tip," *Appl. Phys. Lett.*, vol. 116, no. 24, Jun. 2020, Art. no. 241102.

[29] X. Xu *et al.*, "A miniature fiber collimator for highly sensitive bend measurements," *J. Lightw. Technol.*, vol. 36, no. 14, pp. 2827–2833, Jul. 2018.

[30] H. J. Lezec and T. Thio, "Diffracted evanescent wave model for enhanced and suppressed optical transmission through subwavelength hole arrays," *Opt. Express*, vol. 12, no. 16, pp. 3629–3651, Aug. 2004.

[31] H. Kim *et al.*, "Metallic fresnel zone plate implemented on an optical fiber facet for super-variable focusing of light," *Opt. Express*, vol. 25, no. 24, pp. 30290–30303, Nov. 2017.

Jian Yu received the Ph.D. degree in optical engineering from Chongqing University in 2017. Since March, 2018, he has been with Shenzhen Univeristy, China, as a Postdoctoral Fellow. His current research interests focus on vortex beam.

Cailing Fu received the Ph.D. degree in optical engineering from Shenzhen University, China, in 2018. Since 2015, she has been with Shenzhen University, China, as a Postdoctoral Research Fellow. Her current research interests include optical fiber gratings.

Zhiyong Bai received the Ph.D. degree in optics from Nankai University, China, in 2014. Since 2015, he has been with Shenzhen University, China, as a Postdoctoral Research Fellow. His research interests include optical fiber gratings and orbital angular momentum.

Yiping Wang (Senior Member, IEEE) received the Ph.D. degrees in optical engineering from Chongqing University, China, in 2003. From 2003 to 2005, he was at Shanghai Jiao Tong University, China, as a Postdoctoral Fellow. From 2005 to 2007, he was at the Hong Kong Polytechnic University, as a Postdoctoral Fellow. From 2007 to 2009, he was at the Institute of Photonic Technology, Germany, as a Humboldt Research Fellow. From 2009 to 2011, he was at the Opto-electronics Research Centre, University of Southampton, Southampton, U.K., as a Marie Curie Fellow. Since 2012, he has been with Shenzhen University, China, as a Distinguished Professor.